

Supplemental Information File

Third time's the charm: Intricate non-centrosymmetric polymorphism in $LnSiP_3$ ($Ln = La$ and Ce) induced by distortions of phosphorus square layers

Georgiy Akopov^{1,2,§}, Justin Mark^{1,2,§}, Gayatri Viswanathan^{1,2,§}, Shannon J. Lee^{1,2}, Brennan C. McBride², Juyeon Won^{1,2}, Frédéric A. Perras¹, Alexander L. Paterson¹, Bing Yuan,³ Sabyasachi Sen,³ Adedoyin N. Adeyemi², Feng Zhang^{1,4}, Cai-Zhuang Wang^{1,4}, Kai-Ming Ho^{1,4}, Gordon J. Miller², Kirill Kovnir^{1,2,*}

¹*Ames Laboratory, U.S. Department of Energy, Ames, IA 50011, United States.*

²*Department of Chemistry, Iowa State University, Ames, IA 50011, United States.*

³*Department of Materials Science and Engineering, University of California, Davis, Davis, CA 95616, USA*

⁴*Department of Physics and Astronomy, Iowa State University, Ames, IA 50011, United States.*

§These authors contributed equally

*Corresponding authors: kovnir@iastate.edu

Table of Contents

S1. Experimental Details

S1.1. Synthesis

S1.1.1. Metal Silicide Precursors

S1.1.2. Single Crystals

S1.1.3. Bulk Powders

S1.2. X-ray Diffractions

S1.3. 17-BM *in situ* and 11-BM synchrotron X-ray diffraction

S1.4. Spark Plasma Sintering (SPS)

S1.5. Solid-State Nuclear Magnetic Resonance (SSNMR)

S1.5.1. ^{31}P and ^{139}La SSNMR

S1.5.2. Computational Details for SSNMR

S1.6. Scanning Electron Microscopy and Energy Dispersive Spectroscopy

S1.7. Structure Optimization and Electronic Density of States (DOS)

S1.8. Phonon Density of States (DOS) and Free Energy Calculations

S1.9. Differential Scanning Calorimetry (DSC)

S1.10. Solid-State Diffuse Reflectance Spectroscopy

S1.11. Physical Property Measurements

S.1.12 Raman spectroscopy

Table S1. Single crystal data collection and refinement parameters for LnSiP_3 polymorphs;

Table S2. Experimental and GIPAW-DFT calculated ^{31}P solid-state NMR data;

Figure S1. PXRD patterns for the arc-melted precursors for LnSi ($\text{Ln} = \text{La}$ and Ce);

Figure S2. *In situ* 17-BM PXRD showing phase formation in the CeSiP_3 system;

Figure S3A. 11-BM PXRD and data refinement for LaSiP_3 ($Aea2$);

Figure S3B. 11-BM PXRD and data refinement for LaSiP_3 ($Pna2_1$);

Figure S4. PXRD for LaSiP_3 ($P2_1/c$);

Figure S5. PXRD patterns showing phase formation and polymorphism in LnSiP_3 ($\text{Ln} = \text{Pr}$ and Nd);

Figure S6. PXRD results showing phase transformations for LaSiP_3 ;

Figure S7. DSC curves for LaSiP_3 (*Aea2*) and CeSiP_3 (*Pna2*₁ + *Aea2*) and PXRD spectra;

Figure S8. SEM images of polished samples of the three polymorphs of LaSiP_3 ;

Figure S9. Crystal structures of LaSiP_3 (*Aea2* and *Pna2*₁) with labeled phosphorus positions;

Figure S10. Crystal structure of *P2*₁/*c* LaSiP_3 with labeled phosphorus positions;

Figure S11. La layers in LaSiP_3 (*Pna2*₁ and *Aea2*) projected down [100] and [010] directions;

Figure S12. Relationship between *Pna2*₁ and *Aea2* space groups with corresponding splitting of atomic positions;

Figure S13. Interatomic distances in the pnictogen layer of VASP-relaxed structures for *Pna2*₁ and *Aea2* in LaSiP_3 ;

Figure S14. Calculated DOS for five relaxed models of the *Aea2* polymorph of LaSiP_3 ;

Figure S15. Phonon DOS for *Pna2*₁, *P2*₁/*c*, and fully relaxed *Aea2* model of LaSiP_3 ;

Figure S16. Free energy difference between the *Pna2*₁ and *P2*₁/*c* polymorphs of LaSiP_3 ;

Figure S17. Tauc plots for the indirect transitions in the three polymorphs of LaSiP_3 ;

Figure S18. Raman spectra for *Pna2*₁ and *Aea2* LaSiP_3 polymorphs;

Figure S19. Different representations of P layer in the crystal structure of *Aea2* LaSiP_3 polymorph.

References

S1. Experimental Details

S1.1. Synthesis

The powders of different polymorphs of $LnSiP_3$ ($Ln = La, Ce$) were synthesized using pre-arc-melted precursors and phosphorus without flux, while crystals were grown using either a flux synthesis from elements, non-flux synthesis from a pre-arc-melted precursor or a flux synthesis from a pre-arc-melted precursor. Elemental Si powder (99.99%, Alfa Aesar, USA), Si chips (99.9999%, Strem, USA), red P powder (98.9%, Alfa Aesar, USA), Sn shot (99.8%, Alfa Aesar, USA), La powder (99.7%, Alfa Aesar, USA), La ingot (99.9999%, Ames Lab, USA), Ce ingot (99.9999%, Ames Lab, USA), Sm ingot (99.9999%, Ames Lab, USA), and Gd ingot (99.9999%, Ames Lab, USA) were used as received. Lanthanum, cerium, samarium, and gadolinium pieces were acquired from the Materials Preparation Center at Ames Laboratory, which is supported by the US DOE Basic Energy Sciences.

HAZARD: *The amount of P in any reaction container should be kept to a minimum because at relatively high temperatures during synthesis the resulting vapor pressure of P may be sufficient to cause the sealed ampoule to shatter or explode!*

S1.1.1. Metal Silicide Precursors

Ln -Si precursors were prepared using cut Ln ($Ln = La, Ce, Pr, Sm$ and Gd) pieces and Si chips. Samples with a total mass of 1 g were weighed out in a ratio of $Ln : Si = 1 : 1.05$ to account for evaporation of silicon. The samples were then placed in an arc-melter on a copper hearth along with oxygen getter materials (zirconium metal). The arc-melter chamber was later sealed and evacuated for 20 minutes followed by purging with argon; this process was repeated 3 times to ensure no oxygen was present in the chamber. During arc-melting, the getters were melted first to

ensure the absorbance of any trace oxygen, and then the samples were heated for $T \sim 1$ minute at a current of $I \sim 70$ Amperes (A) until molten, allowed to solidify, flipped and re-arc'd 2 more times to ensure homogeneity under a current of $I \sim 120$ A. The precursor ingots were then crushed into a powder using a tool steel Plattner-style diamond crusher.

S.1.1.2. Single Crystals

Single crystals of LaSiP_3 ($P2_1/c$) were synthesized by loading La, Si, P, and Sn into a carbonized silica ampoule in a 1:1:7.5:16 molar ratio, respectively. A plug of silica wool was then loaded into the ampoule slightly above the sample. The ampoule was flame sealed under vacuum and placed in a muffle furnace. The sample was heated to 800 °C over 17 h and annealed at this temperature for 168 h. The sample was then centrifuged from this temperature.

Crystals of LaSiP_3 ($Pna2_1$) were synthesized in a similar manner as LaSiP_3 ($P2_1/c$). However, rather than elemental La and Si, an arc melted LaSi precursor was used. LaSiP_3 was synthesized by heating the sample to 1050 °C over 17 h and annealing at this temperature for 24 h. The sample was slow cooled to 800 °C over 24 h and annealed at this temperature for 48 h before centrifugation to remove Sn flux.

Crystals of LaSiP_3 ($Aea2$) were synthesized using a stoichiometric combination of the pre-synthesized LaSi binary and P in a 1 : 3 ratio without Sn flux. The sample was heated in a carbonize ampoule to 1050 °C over 14 h and the furnace was turned off and allowed to cool naturally to room temperature.

Crystals of CeSiP_3 (both $Pna2_1$ and $Aea2$) were synthesized by loading elemental Ce, Si, P and Sn into a carbonized silica ampoule in a 1:1:7.5:16 molar ratio, respectively. A plug of silica wool was loaded into the ampoule slightly above the sample. The ampoule was flame sealed under

vacuum and was then heated to 1000 °C over 17 h and annealed at this temperature for 24 h. The sample was then cooled over 24 h to 800 °C and annealed at this temperature for 48 h before the sample was centrifuged to remove Sn flux from the sample. The resulting sample contains a mixture of crystals of both polymorphs.

S.1.1.3. Bulk Powders

Bulk powders of the materials were synthesized using arc-melted $LnSi$ precursors and phosphorus. Samples were prepared by loading the silicide binary and phosphorus in a silica ampoule in a 1 : 3 precursor to phosphorus ratio. The ampoules were then flame sealed under vacuum. $Aea2$ polymorphs were synthesized by heating samples over 14 h to 1050 °C (1000 °C in case of Pr and Nd) and then allowing them to cool to room temperature over 10 h with no dwell time at maximum temperature. $Pna2_1$ polymorphs were synthesized by heating the sample to either 750 °C ($LaSiP_3$, $PrSiP_3$, and $NdSiP_3$) or 900 °C ($CeSiP_3$) over 14 h and annealing at this temperature for 240 h before allowing the sample to cool to room temperature. Bulk $LaSiP_3$ ($P2_1/c$) was similarly synthesized by heating to 900 °C over 12 h and annealing at this temperature for 240 h before shutting off the furnace.

S1.2. X-ray Diffraction

Powder X-ray diffraction (PXRD) was performed using a Rigaku Miniflex 600 with $Cu-K_\alpha$ radiation and a $Ni-K_\beta$ filter. Sample holders were composed of zero-background silicon plates.

Single crystal X-ray diffraction (SCXRD) was performed using a Bruker D8 Venture diffractometer using $Mo-K_\alpha$ radiation. The $LaSiP_3$ ($Pna2_1$ and $Aea2$) datasets were collected at 100 K and the $CeSiP_3$ ($Aea2$) dataset at 200 K under a N_2 stream; $CeSiP_3$ ($Pna2_1$) and $LaSiP_3$ ($P2_1/c$) datasets were collected at 293 K. All datasets had ω -scans recorded at a 0.3° step width and were

integrated with the Bruker SAINT software package. Structure determination and refinement of the crystal structures were carried out using the SHELX suite of programs.¹

In all crystal structures, the Si and P sites were identified based on analysis of site occupancy factors and coordination, assuming Si occupies the center of P₄ tetrahedron. The compositions obtained were confirmed by EDS elemental analysis. For the crystal structure of *P2₁/c* polymorph all atomic sites were found to be fully occupied. The same was true for *Pna2₁* polymorphs, and all the attempts to solve these structures in the centrosymmetric space group *Pbcn* were unsuccessful. Low values of Flack parameter confirm the NCS nature of the crystal structure (**Table S1**). Final refinements were performed accounting for racemic twinning of the crystals. Analogously, all attempts to solve the structure of *Aea2* polymorphs in the centrosymmetric space group *Cmce* were unsuccessful (**Table S1**). In the crystal structures of *Aea2* polymorphs, substantial disorder in the square P layer was found. In the final refinement, three or four P split sites were refined with the constraint of isotropic atomic displacement parameters and total occupancy of 100%. Additionally, small disorder in the Si-P tetrahedral layer was found as described in the main text.

S1.3. Synchrotron Experiments at Advanced Photon Source at Argonne National Laboratory (APS ANL)

In situ variable temperature powder X-ray diffraction experiments were carried out at the 17-BM beamline at APS ANL, $\lambda = 0.24158 \text{ \AA}$. To study the mechanism of formation of *LnSiP₃*, a small amount of precursor (LaSi or CeSi) was ground in an agate mortar with P in 1:3 ratio, loaded in a 0.5mm (ID) capillary, and sealed under vacuum using a flame. For synthesis experiments, the following profile was used: heating at 50 °C/min to 900 °C, hold 5 minutes, cooling at 25 °C/min to 750 °C, cooling at 50 °C/min to 500 °C, and then cooling at 100 °C/min to room temperature. To study polymorphic transformations, a small amount of the pre-synthesized phase (CeSiP₃

Pna2₁) was ground in an agate mortar, put in a 0.5mm (ID) capillary, and sealed under vacuum using a flame. For the transformation experiment, the following profile was used: heating at 50 °C/min to 500 °C, heating at 10 °C/min to 950 °C, hold 15 minutes, heating at 10 °C/min to 1000 °C, hold 15 minutes, then cooling at 100 °C/min to room temperature. The 11-BM beamline at APS ANL was utilized for high-resolution room temperature PXRD experiments. For these experiments, a small amount of the synthesized polymorphs of LaSiP₃ were ground in an agate mortar with silica powder in a 1 : 13 ratio and loaded in Kapton capillary tubes. Data analysis was performed using the GSAS II software.²

S.1.4. Spark Plasma Sintering (SPS)

High density pellets of 5 mm diameter were pressed using a Dr. Sinter Lab Jr. SPS-211Lx. Samples were ground into a fine powder and loaded in a graphite die between graphite foil and tungsten carbide plungers. This die was then loaded into a larger die with graphite plungers as a protective outer jacket. For *Aea2* polymorphs, pellets were sintered under a partial argon atmosphere by heating to 500 °C over 5 minutes under 51 MPa of pressure, followed by heating to 750 °C over 15 minutes and annealing at this temperature for 10 minutes. Pressure was gradually increased over time beginning at 550 °C to reach a maximum of 158 MPa at 750 °C. LaSiP₃ (*Pna2₁*) pellets were sintered under partial argon atmosphere by heating to 500 °C over 5 minutes under 51 MPa of pressure, followed by heating to 650 °C over 15 minutes and annealing at this temperature for 10 minutes. Pressure was gradually increased over time beginning at 500 °C to reach a maximum of 204 MPa at 650 °C. CeSiP₃ (*Pna2₁*) pellets were sintered under partial argon atmosphere by heating to 500 °C over 5 minutes under 51 MPa of pressure, followed by heating to 700 °C over 15 minutes and annealing at this temperature for 10 minutes. Pressure was gradually increased over time beginning at 500 °C to reach a maximum of 255 MPa at 700 °C. After annealing, pressure

was released, and the sample was cooled to room temperature. The pellet was removed from the graphite die and polished to remove any traces of graphite. The geometrical densities of the pellets were determined to be 91-95 % for LaSiP_3 (*Aea2* and *Pna2*₁) and CeSiP_3 (*Aea2*); and 80% for CeSiP_3 (*Pna2*₁). In the last case, higher temperatures could not be used for pressing as the sample transforms from *Pna2*₁ to *Aea2* polymorph at sintering temperatures above 650 °C.

S1.5. Solid-State Nuclear Magnetic Resonance (SSNMR)

S1.5.1. ³¹P and ¹³⁹La SSNMR

All solid-state NMR experiments were performed on a 600 MHz Varian NMR System equipped with a 1.6-mm triple-resonance fast-MAS probe. Hahn echo and MAT experiments used 100 kHz ³¹P radiofrequency (rf) pulses and a MAS spinning frequency of 36 kHz, while the rf power was reduced to 83 kHz for the TRAPDOR measurements due to the lowered efficiency of the probe while in triple-resonance mode. Relaxations delays were set to 2 s, with the exception of the *Pna2*₁ sample for which they were increased to 8 s. Hahn echo experiments used echo delays lasting 1 rotor period (27.8 μs) and 128 scans were accumulated for the *Pna2*₁ and *P2*_{1/c} samples while 256 were acquired for the *Aea2* sample. Two-dimensional magic-angle-turning NMR experiments were performed using the 5π sequence³ and used a constant time period lasting 43 rotor periods. A total of 256 t_1 increments were acquired with the indirect spectral width set to 170 kHz. The 56 first t_1 increments were effectively decrements and were aimed at acquiring the full MAT echo to obtain pure phase 2D lineshapes. 11 scans were accumulated for the *Pna2*₁ and *P2*_{1/c} polymorphs and 33 were accumulated for the *Aea2* sample. Sign discretion in the indirect dimension was obtained with the use of States-TPPI. The two-dimensional DQ/SQ spectrum of the *Pna2*₁ polymorph was acquired using 8 rotor periods of BaBa⁴ double-quantum recoupling. A total of 48 t_1 increments of 27.8 μs, each consisting of 256 scans, were acquired with States-TPPI. For the

$^{31}\text{P}\{^{139}\text{La}\}$ TRAPDOR^{5,6} experiments, the echo delays were incremented by 27.8 μs (dephasing time increments of 55.5 μs) and a total of 20 increments were acquired. The ^{139}La power and offset were optimized to maximize the dephasing. 384, 512, and 128 scans were acquired for each of these increments for the *Aea2*, *P2₁/c*, and *Pna2₁* polymorphs, respectively.

S1.5.2. Computational Details for SSNMR

Density functional theory (DFT) calculations were carried out using the CASTEP package (version 2018).⁷ NMR calculations were carried out using the GIPAW module as implemented within CASTEP.^{8,9} To enable the calculation of NMR parameters, which require an explicit treatment of the electronic environment near the nucleus, ultrasoft pseudopotentials (USPP) were used.¹⁰ In particular, USPP were generated using the “on-the-fly” routine contained within CASTEP using the default generation scripts.

All calculations were carried out using the PBEsol exchange-correlation functional.¹¹ A plane-wave cutoff energy of 400 eV was found to be sufficient to converge calculated isotropic magnetic shielding constants to a value of less than 1 ppm. Monkhort-Pack grids with spacing of approximately 0.008 \AA^{-1} were used, corresponding to a $28 \times 10 \times 16$ grid for the *P2₁/c* polymorph and a $20 \times 12 \times 20$ grid for the *Pna2₁* polymorph. This is an extremely fine grid spacing but proved necessary to converge the ^{31}P isotropic magnetic shielding constants. Self-consistent field tolerances were set to 1.0×10^{-6} eV/atom, which proved more than sufficient. To assign them, we performed gauge-including projector augmented-wave (GIPAW)¹²⁻¹⁴ density functional theory (DFT) calculations of the ^{31}P magnetic shielding tensors which were later converted to chemical shifts using the shielding calculated for GaP as an external reference.^{15,16}

NMR calculations were performed on the experimental structure, the experimental structure with ionic positions allowed to relax, and fully optimized (lattice constants and ionic positions) structures for each phase. Geometry optimization was conducted with maximum force tolerances of 0.03 eV/atom, maximum displacement tolerances of 1.0×10^{-3} Å/atom, and for the full optimization, maximum stress tolerance of 0.05 GPa. The average difference in ^{31}P isotropic shielding between experimental and fully optimized structures was approximately 2 ppm, with the shielding constants of the ionic relaxation structure typically falling in between. The reported values are from the structure using experimental lattice constants with relaxed ionic positions.

The calculated magnetic shielding constant of ^{31}P in GaP was used to define the chemical shift scale, with GaP having an experimental chemical shift of -145 ppm relative to 85% phosphoric acid^{15,16} ($\sigma_{ref} = 368.06$ ppm).

S.1.6. Scanning Electron Microscopy/Energy Dispersive Spectroscopy (SEM/EDS)

Elemental analysis of samples was conducted using a FEI Quanta 250 field emission-SEM with EDS detector (Oxford X-Max 80, ThermoFischer Scientific, Inc., USA) and analyzed using the Aztec software. Powder samples were mounted in epoxy, polished to a level surface, and coated with a conductive layer of carbon.

S.1.7. Structure Optimization and Electronic Density of States (DOS)

DFT calculations were performed employing the plane-wave basis sets in the Vienna ab initio simulation package (VASP).^{17,18} Projector-augmented-wave (PAW) pseudopotentials and Perdew-Burke-Ernzerhof (PBE) generalized gradient functionals were employed to determine the optimized electronic structure and density of states (DOS) of all three polymorphs for LaSiP_3 .¹⁹⁻²¹ All calculations used an energy cutoff of 500 eV and Γ -centered k -point meshes for integration of

the irreducible wedge of the first Brillouin zone using the linear tetrahedron method. $24 \times 8 \times 12$, $16 \times 4 \times 16$, and $16 \times 4 \times 16$ k-meshes were employed to study the $P2_1/c$, $Pna2_1$, and $Aea2$ polymorphs of LaSiP_3 , respectively.^{22,23}

The electronic structures of LaSiP_3 polymorphs were evaluated after relaxation. The self-consistent electronic optimization converged when the energy change was less than 1×10^{-4} eV, and the ionic relaxation terminated when the force on each atom is less than 0.02 eV/Å. The crystal structures determined from single crystal X-ray diffraction were used as initial structures for the $P2_1/c$ and $Pna2_1$ polymorphs. These structures were allowed to relax freely for complete optimization of the unit cell and atomic positions. The symmetry of the resulting structures were evaluated using FINDSYM in the ISOTROPY software suite before calculating the density of states (DOS).^{24,25} Complete relaxation of the unit cell and atomic positions of the $P2_1/c$ and $Pna2_1$ polymorph did not result in any significant distortions or changes to the crystal structure. The DFT-optimized lattice parameters ($P2_1/c$: $a = 4.3527$ Å, $b = 12.8610$ Å, $c = 7.9051$ Å, $\beta = 93.6368^\circ$; $Pna2_1$: $a = 5.9803$ Å, $b = 25.5388$ Å, $c = 5.7835$ Å) and atomic positions agree well with those determined experimentally.

The crystallographic disorder in the pnictogen layer of the $Aea2$ polymorph poses a challenge for DFT calculations. To circumvent this issue, several ordered models were developed based on the experimentally determined crystal structure. All five constructed models have the same $Aea2$ symmetry as the disordered crystal structure and assume full occupancy of the Si1 and P1 sites, but differ from one another in terms of their pnictogen layers. These models were relaxed and compared to evaluate the electronic structure of the $Aea2$ polymorph. The first model featured an ordered rectangular net of P atoms and was relaxed either partially or completely. The partial relaxation allowed for optimization of unit cell size and shape but retained atomic coordinates of

the initial structure. The complete relaxation allowed for free optimization of the unit cell and atomic positions. The next three models have pnictogen layers that assume one of the 3 partially occupied P sites in the experimental crystal structure (P31, P32, or P33) are completely occupied. These models were relaxed partially to retain the atomic positions but allow for unit cell contraction or expansion. The interatomic distances within the pnictogen layer of these relaxed models are given in **Figure S13**.

S1.8. Phonon Density of States (DOS) and Free Energy Calculations

To further examine the stability of the LaSiP₃ polymorphs, phonon calculations were performed using the Phonopy package.²⁶ Since phonon calculations are more sensitive to energy and force convergence, the tolerance for the self-consistent energy and the ionic force were set to more strict values of 1 x 10⁻⁸ eV and 0.005 eV/Å, respectively. For the *Aea2* polymorph with partial occupancy, only the fully relaxed model (**Figure S13, S14**) was examined because phonon calculations require a fully relaxed structure with vanishing atomic forces.

The phonon contributions to the free energy at finite temperatures were also calculated within the quasi-harmonic approximation for the two stable polymorphs *P2₁/c* and *Pna2₁*.²⁶ The free energy is given by

$$F = E_0 + k_B T \sum_{n\mathbf{k}} \ln \left[2 \sinh \frac{\hbar \omega_{n\mathbf{k}}}{2k_B T} \right],$$

where E_0 is the 0 K total energy from VASP calculations and $\omega_{n\mathbf{k}}$ is the dispersion relation for the phonon bands. To account for the thermal expansion at finite temperatures, phonon spectra $\omega_{n\mathbf{k}}$ were calculated at various volumes and the free energy was minimized with respect to volume.

In order to interpret the Raman spectrum for the $Pna2_1$ polymorph, the frequencies and eigenvectors of the zone-center optimal phonon modes were calculated using the “frozen phonon” method as implemented in VASP. The atoms are successively displaced by ± 0.015 Å along all Cartesian axes. The dynamical matrix is then constructed from the forces on each atom based on finite differences.

S.1.9. Differential Scanning Calorimetry (DSC)

DSC was performed using a Netzsch DSC 404 F3 Pegasus (Mettler Toledo, USA). Approximately 20 mg of pure polycrystalline sample was sealed into an evacuated silica ampoule and measured against a blank. Both heating and cooling profiles were collected using a 10 °C/min rate from 25 to 1100 °C.

S1.10. Solid-State Diffuse Reflectance Spectroscopy

Solid-state UV-Vis spectroscopy measurements were taken on a Perkin Elmer Lambda 1050+ UV/Vis/NIR spectrometer equipped with a 150 mm Spectralon-coated integrating sphere. Finely ground black powders were loaded into a spherical powder sample holder, pressed against the lens, and held in place by a spring. The holder was then placed at the reflectance port while the specular port was left open. The iris aperture was adjusted so the sample beam was focused only on the samples and a Spectralon reference standard was used as a blank. Kubelka-Munk conversion of the diffuse reflectance data was used to determine the bandgaps of all three LaSiP_3 polymorphs. Tauc plots were constructed to evaluate the direct and indirect band gaps of the phases.

S1.11. Physical Property Measurements

Transport properties were measured using a Quantum Design Physical Property Measurement System. Thermal conductivity was measured using the Thermal Transport Option in a two-probe

configuration. Electrical resistivity was measured using the Alternating Current Transport option and a four-probe geometry using 50 μm platinum wires and silver paste.

S1.12. Raman Spectroscopy

The unpolarized Raman spectra of the *Aea2* and the *Pna2₁* polymorphs of LaSiP_3 were collected in backscattering geometry with a resolution of 1 cm^{-1} , using a Renishaw RM 1000 Raman Microscope System equipped with an edge filter for Rayleigh rejection and a confocal microscope. Diode lasers operating at wavelengths of 785 nm (*Aea2* polymorph) and 633 nm (*Pna2₁* polymorph) were used for excitation and a 50x objective lens with a working distance of 0.37 mm was used to focus the laser light on the sample. Backscattered light was detected using a charge coupled device detector cooled at 200 K.

Table S1. Single crystal data collection and refinement parameters for $LnSiP_3$ polymorphs ($Ln = La$ and Ce).

	LaSiP₃	CeSiP₃	LaSiP₃	CeSiP₃	LaSiP₃
CSD-number	2051283	2051285	2051281	2051284	2051282
Space group	<i>Pna2₁</i>		<i>Aea2</i>		<i>P2₁/c</i>
λ (Å)	Mo-K α : 0.71073				
<i>T</i> (K)	100(2)	293(2)	100(2)	200(2)	293(2)
<i>a</i> (Å)	5.9078(3)	5.8633(3)	5.9650(2)	5.8961(3)	4.3162(2)
<i>b</i> (Å)	25.438(1)	25.314(1)	25.213(1)	25.099(1)	12.8090(7)
<i>c</i> (Å)	5.7398(2)	5.7097(3)	5.8168(2)	5.7747(2)	7.8719(5)
β (°)	-	-	-	-	93.671(2)
<i>V</i> (Å³)	862.60(6)	847.46(7)	874.80(5)	854.57(6)	434.31(4)
<i>Z</i>	8	8	8	8	4
ρ (g•cm⁻³)	4.00	4.09	3.95	4.06	3.98
Absorption correction	numerical	numerical	multiscan	multiscan	multiscan
μ (mm⁻¹)	11.07	11.93	10.92	11.83	11.00
θ (°)	3.20 - 27.72	3.57 - 27.51	3.23 - 27.54	3.82 - 27.50	4.11 - 27.48
Data / param.	1904/93	1930/93	1009/64	979/65	997/46
<i>R</i>₁	0.017	0.014	0.018	0.027	0.019
<i>wR</i>₂	0.039	0.035	0.049	0.062	0.038
Goodness-of-fit	1.21	1.32	1.18	1.15	1.10
Flack Param.	0.33(2)	0.22(2)	0.25(4)	0.07(5)	-
Diff. peak/hole (e•Å⁻³)	0.75/-1.22	1.04/-0.83	1.07/-0.85	1.03/-1.48	1.16/-0.92

Table S2. Experimental and GIPAW-DFT calculated ^{31}P solid-state NMR data.

Polymorph	site	$\delta_{\text{iso,expt.}} / \text{ppm}$	$\sigma_{\text{iso,calc.}} / \text{ppm}$	$\delta_{\text{iso,calc.}} / \text{ppm}^{\text{a}}$	$\Omega_{\text{calc.}} / \text{ppm}^{\text{b}}$	$\kappa_{\text{calc.}}^{\text{b}}$	$T_1^{\text{c}} / \text{s}$
<i>Pna2₁</i>	P1	-190	441.8	-218.8	232.8	-0.07	26.5,
	P2	85	152.0	71.0	631.9	0.52	11.1,
	P3	-12	301.6	-78.6	174.8	0.14	39.2
	P4	40	212.7	10.4	578.7	0.76	high
	P5	-170	424.5	-201.5	215.0	-0.16	to low
	P7	5	283.3	-60.2	202.5	0.26	frequency
<i>Aea2</i>	P1	-175					2.2
	P2	~17					2.2
	P31/P32/P33/P44	46					2.2
<i>P2₁/c</i>	P2	42	221.55	1.51	446.1	0.56	4.1
	P3	-172	329.05	-105.99	354.9	0.13	3.4
	P4	-172	330.11	-107.05	329.5	0.17	3.4

^a DFT calculated magnetic shielding constants (σ) were converted to chemical shifts (δ), with respect to phosphoric acid, using an absolute shielding value of 368.06 ppm obtained through a calculation of the shielding constant of phosphorus in GaP.^{15,16} ^b The anisotropy of the magnetic shielding tensors is reported using the span ($\Omega = \sigma_{33} - \sigma_{11}$) and skew ($\kappa = 3(\sigma_{\text{iso}} - \sigma_{22}) / \Omega$), where principal tensor components are ordered as $\sigma_{33} \geq \sigma_{22} \geq \sigma_{11}$. ^c T_1 relaxation time is for measurements at room temperature.

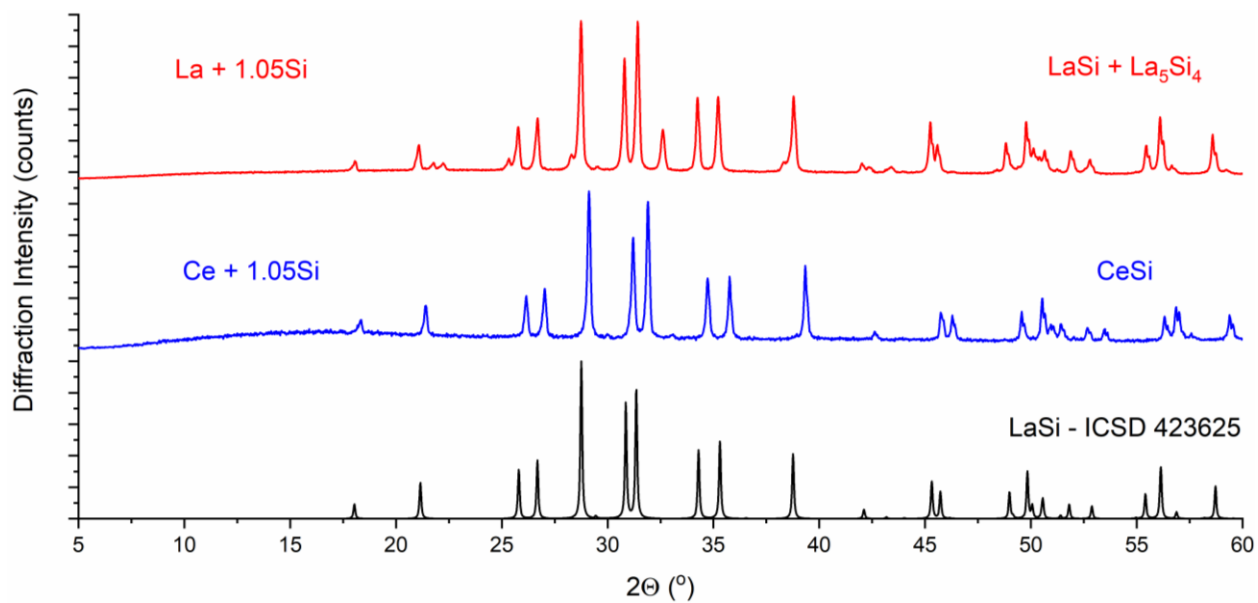


Figure S1. Experimental (red and blue) PXRD patterns for the arc-melted precursors for $LnSi$ ($Ln = La$ and Ce) with a nominal composition of $Ln : Si = 1 : 1.05$. Calculated pattern for $LaSi$ is shown as black line on the bottom. Additional peaks in the $LaSi$ sample correspond to La_5Si_4 .

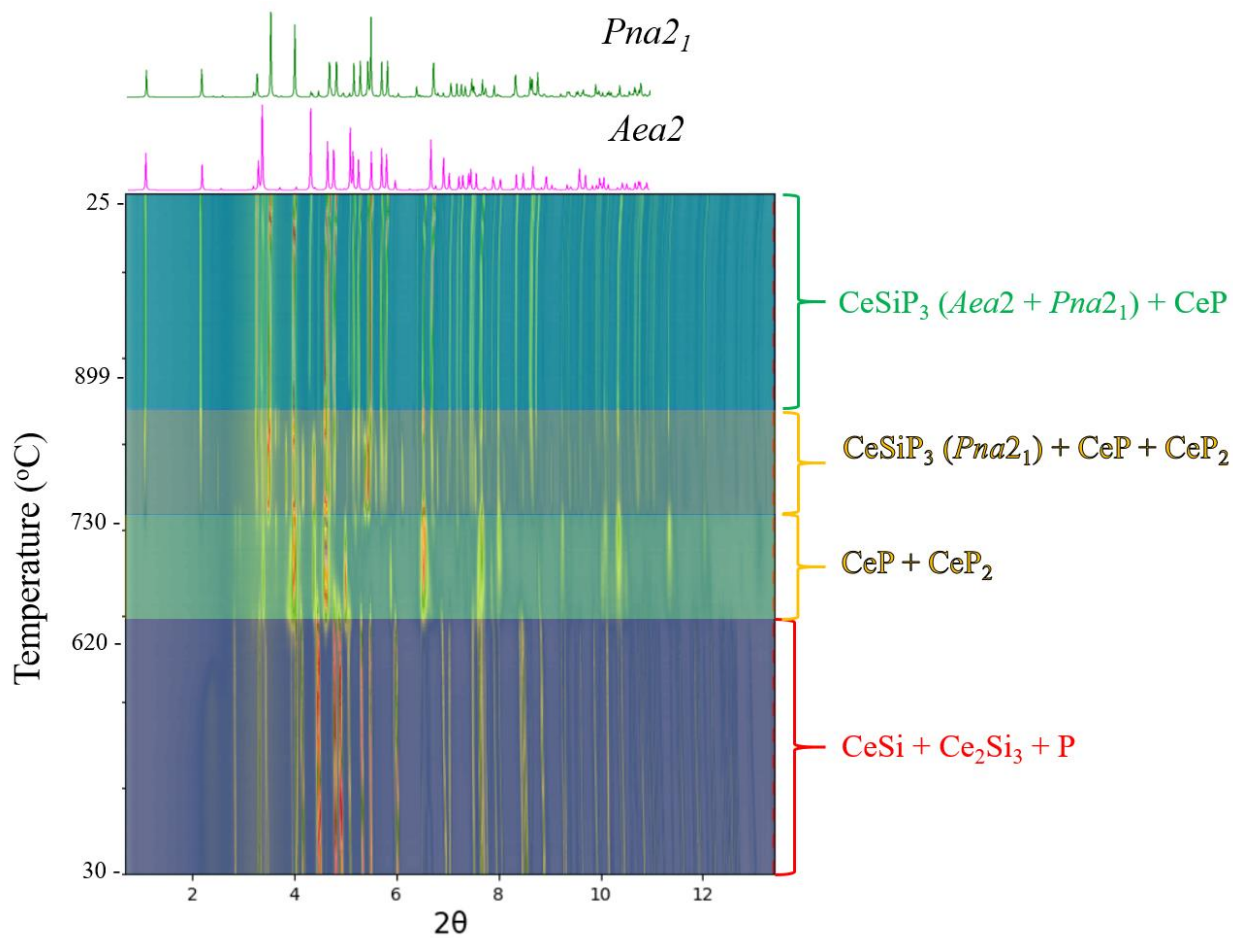


Figure S2. *In situ* PXRD showing phase formation in the CeSiP₃ system collected at the 17-BM beamline at Argonne National Lab. The CeSi and P reactants react to form CeSiP₃ (*Pna2*₁) at 735 °C, followed by a transformation to CeSiP₃ (*Aea2*) above 840 °C. Synchrotron X-ray wavelength $\lambda = 0.24158 \text{ \AA}$.

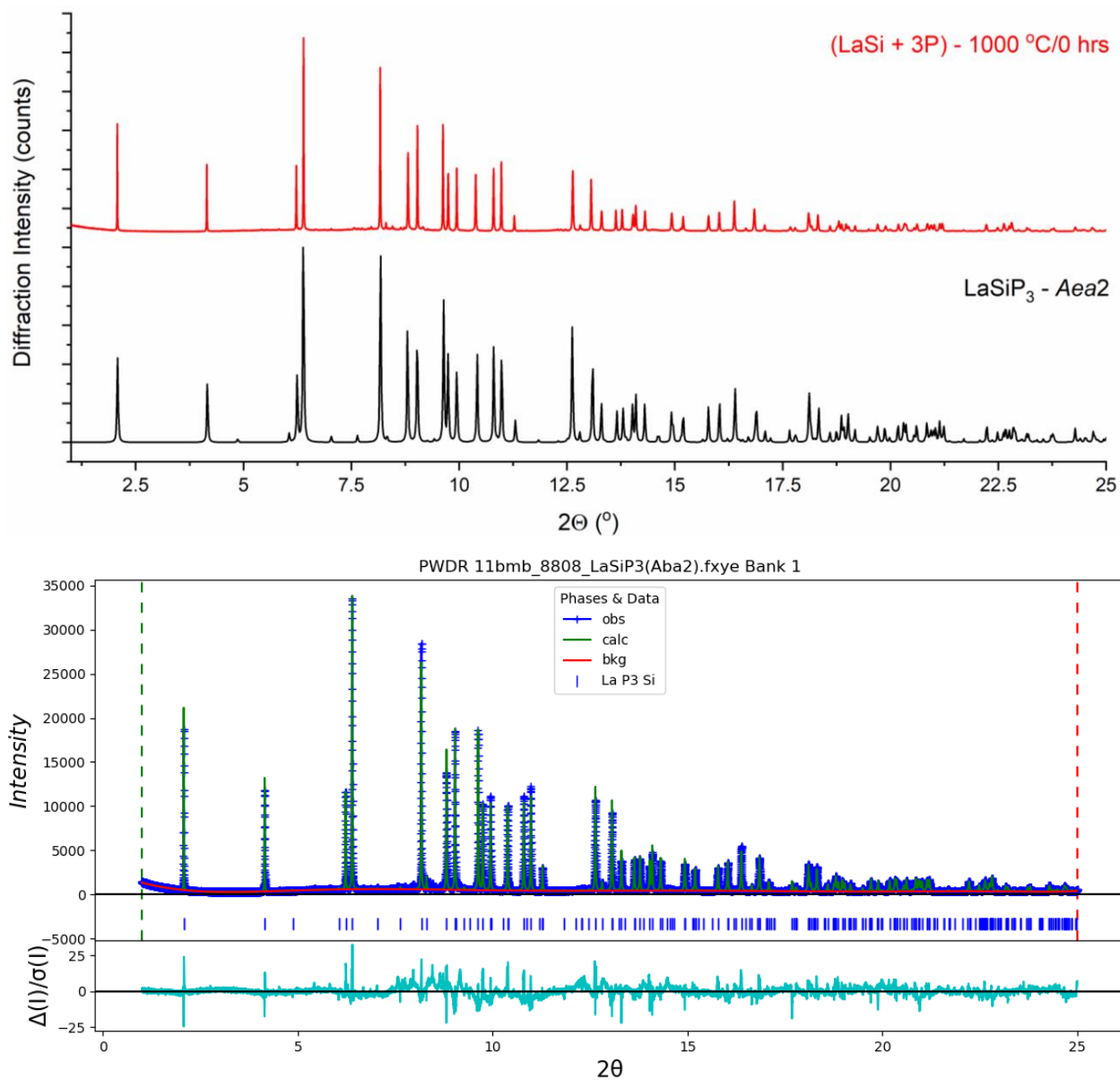


Figure S3A. Synchrotron PXRD patterns and Rietveld refinement (using *GSAS II*)² of LaSiP_3 (*Aea2*) collected at the 11-BM beamline at Argonne National Lab, $\lambda = 0.457842 \text{ \AA}$. In the top panel experimental pattern shown in red while pattern calculated from single crystal diffraction data shown in black.

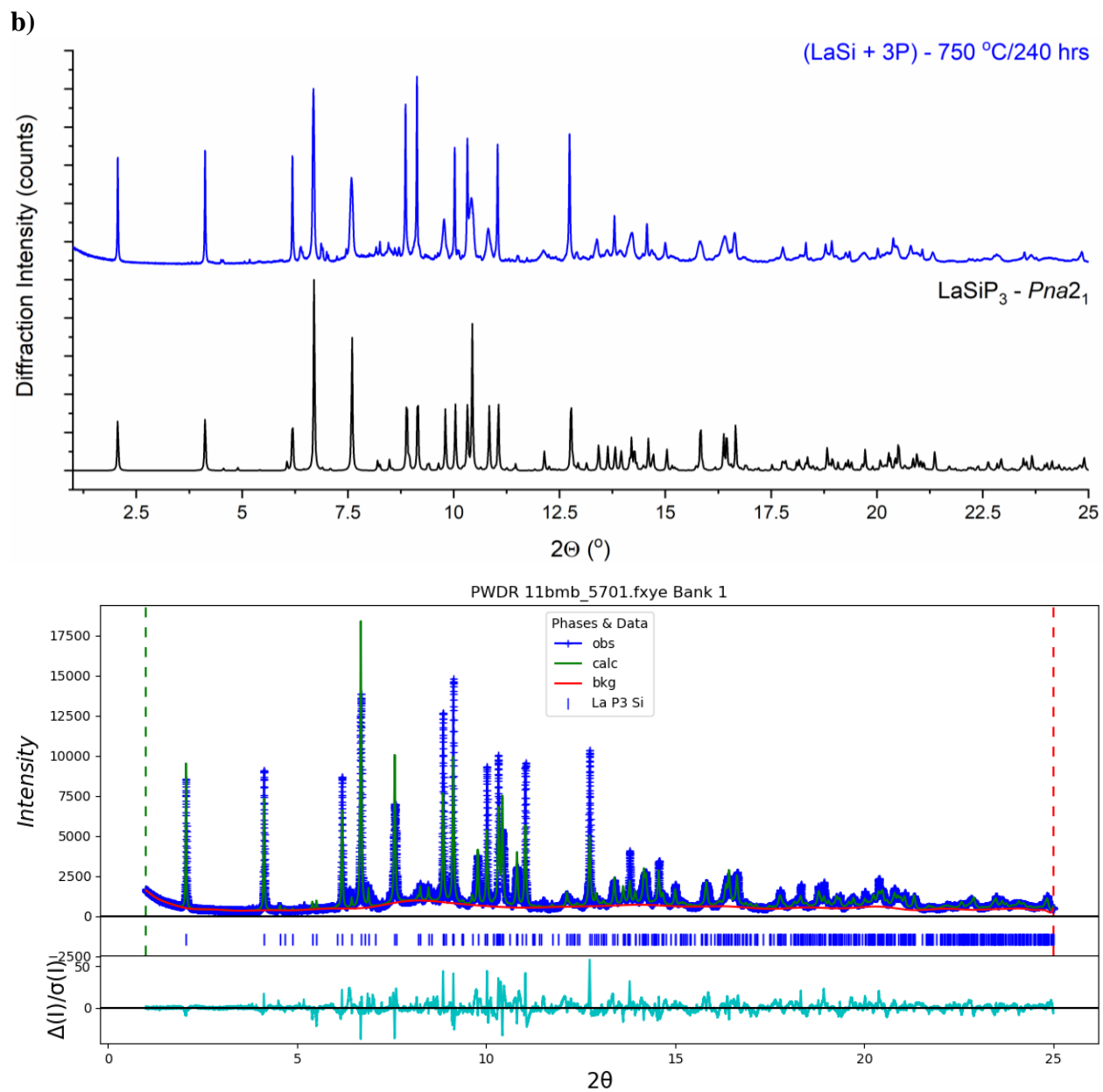


Figure S3B. Synchrotron PXRD patterns and Rietveld refinement (using *GSAS II*)² of LaSiP₃ (*Pna*2₁) collected at the 11-BM beamline at Argonne National Lab, $\lambda = 0.457842$ Å. In the top panel experimental pattern shown in blue while pattern calculated from single crystal diffraction data shown in black.

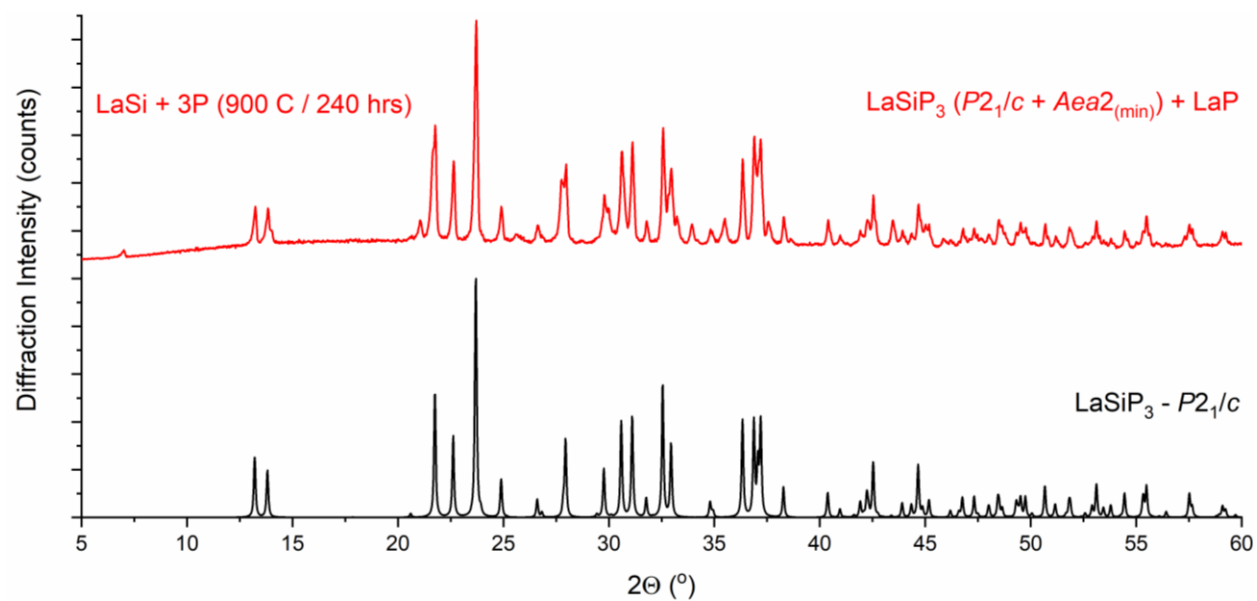


Figure S4. Experimental (red) and calculated (black) PXRD patterns for LaSiP₃ (P_{21/c}) synthesized at 900 °C with a dwell time of 240 h.

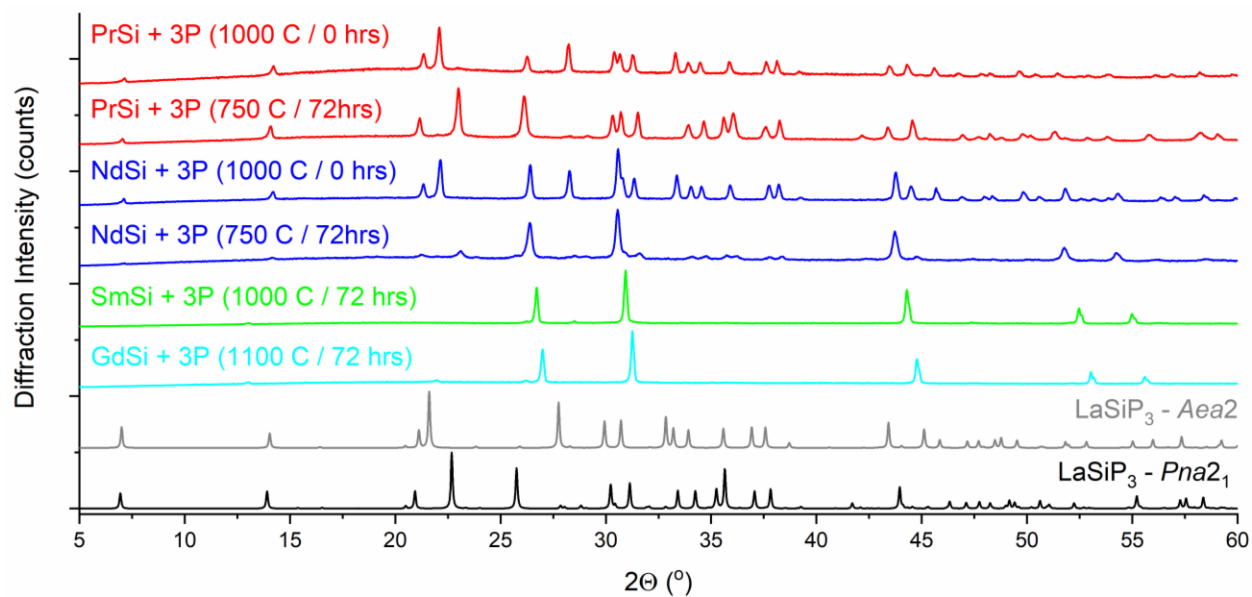


Figure S5. PXRD patterns showing phase formation and polymorphism in $LnSiP_3$ ($Ln = Pr$ and Nd). Aea_2 polymorphs for both lanthanides were synthesized at 1000 °C with no dwell time, while the Pna_2_1 polymorphs was synthesized at 750 °C with a dwell time of 72 hrs. For Sm and Gd, no ternary phase formation was observed; in both cases the products were LnP and SiP . Patterns in black and gray are calculated from the single crystal structures; patterns in color are experimental.

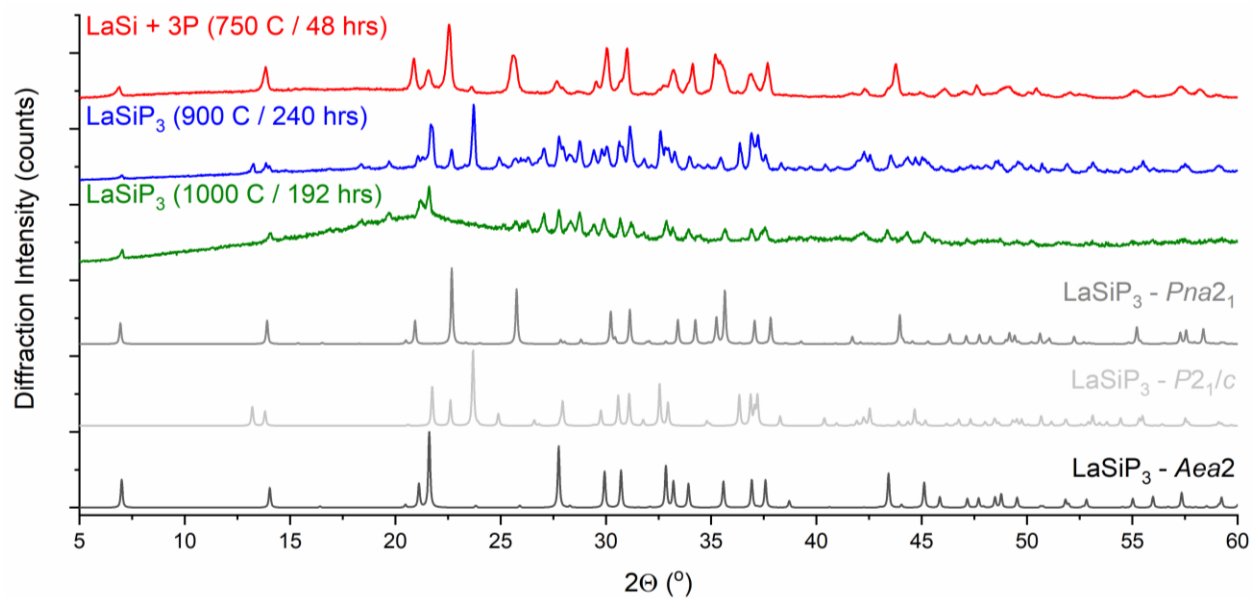


Figure S6. PXRD results showing phase transformations for LaSiP₃ observed via laboratory experiments. The initial *Pna*₂₁ phase (red pattern) was synthesized at 750 °C with a 48 hrs dwell time. A *Pna*₂₁ to *P*₂₁/*c* transformation was achieved with reannealing at 900 °C over 240 hrs (blue pattern), while the transformation to *Aea*₂ occurred with reannealing at 1000 °C over 192 hrs (green pattern). Patterns in color are experimental, patterns in gray and black are calculated from single crystal data.

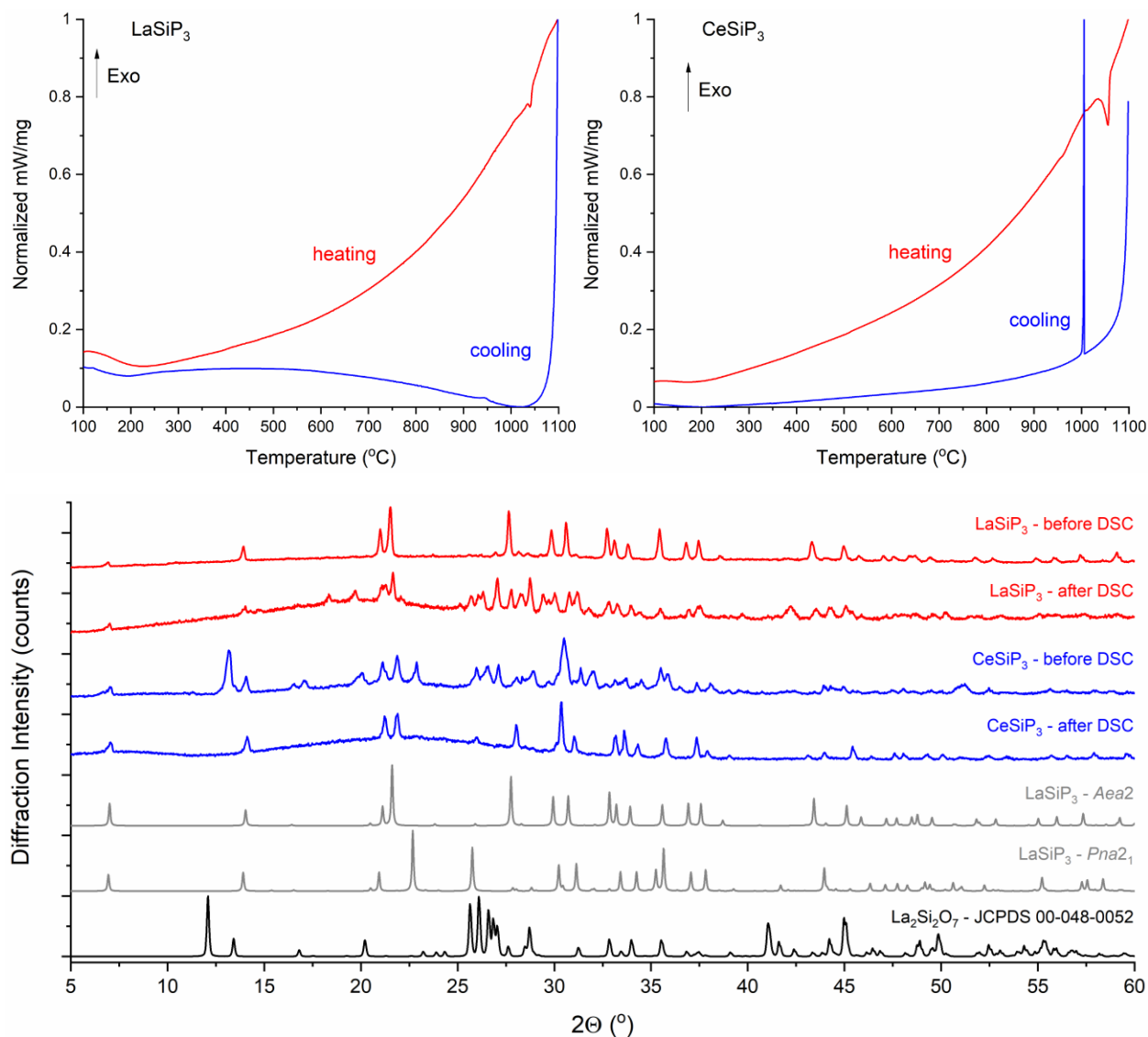


Figure S7. (Top) DSC curves for (left) LaSiP₃ (*Aea2*) and (right) CeSiP₃ (*Pna2*₁ + *Aea2*). Upon heating, a peak at 1035 and 1033 °C are observed for LaSiP₃ and CeSiP₃, respectively, corresponding to an endothermic event. For LaSiP₃, upon cooling a slight exothermic peak at 952 °C is observed. For CeSiP₃, upon cooling an exothermic crystallization peak at 1011 °C is observed. **(Bottom)** PXRD patterns for samples of LaSiP₃ and CeSiP₃ before and after DSC experiments. For LaSiP₃, after DSC, formation of peaks corresponding to La₂Si₂O₇ were observed indicating a reaction of the molten sample with the silica DSC ampoule. For CeSiP₃, after DSC, only peaks corresponding to the *Aea2* polymorph can be seen.

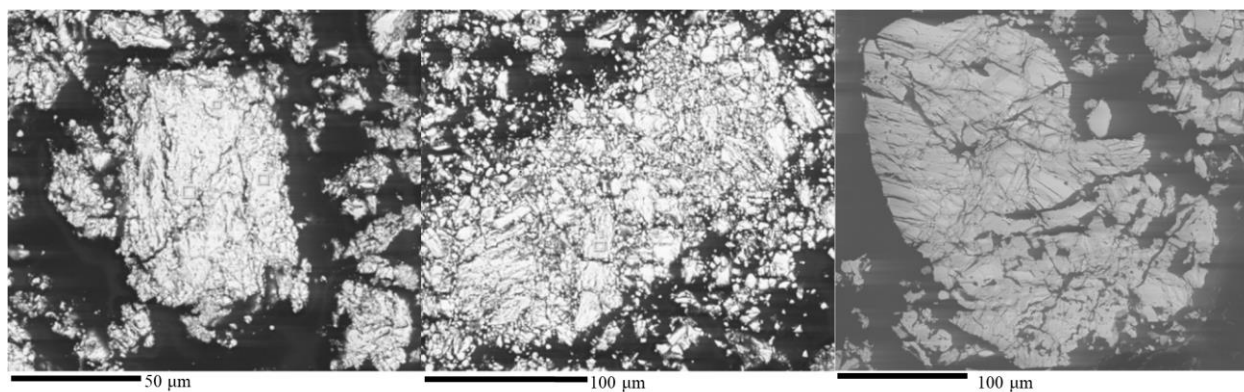


Figure S8. SEM backscattered electron images of polished samples of the three polymorphs of LaSiP_3 . Average compositions are normalized to 1 La atom. **(left)** Aea_2 taken under a magnification of 800x (scale bar is 50 μm) with an average composition of $\text{La}_{1.00}\text{Si}_{1.11(3)}\text{P}_{2.95(6)}$; **(middle)** Pna_2_1 taken at a magnification of 500x (scale bar is 100 μm) with an average composition of $\text{La}_{1.00}\text{Si}_{1.02(2)}\text{P}_{2.87(9)}$; and **(right)** $P2_1/c$ taken at a magnification of 400x (scale bar is 100 μm) with an average composition of $\text{La}_{1.00}\text{Si}_{1.04(7)}\text{P}_{2.71(9)}$.

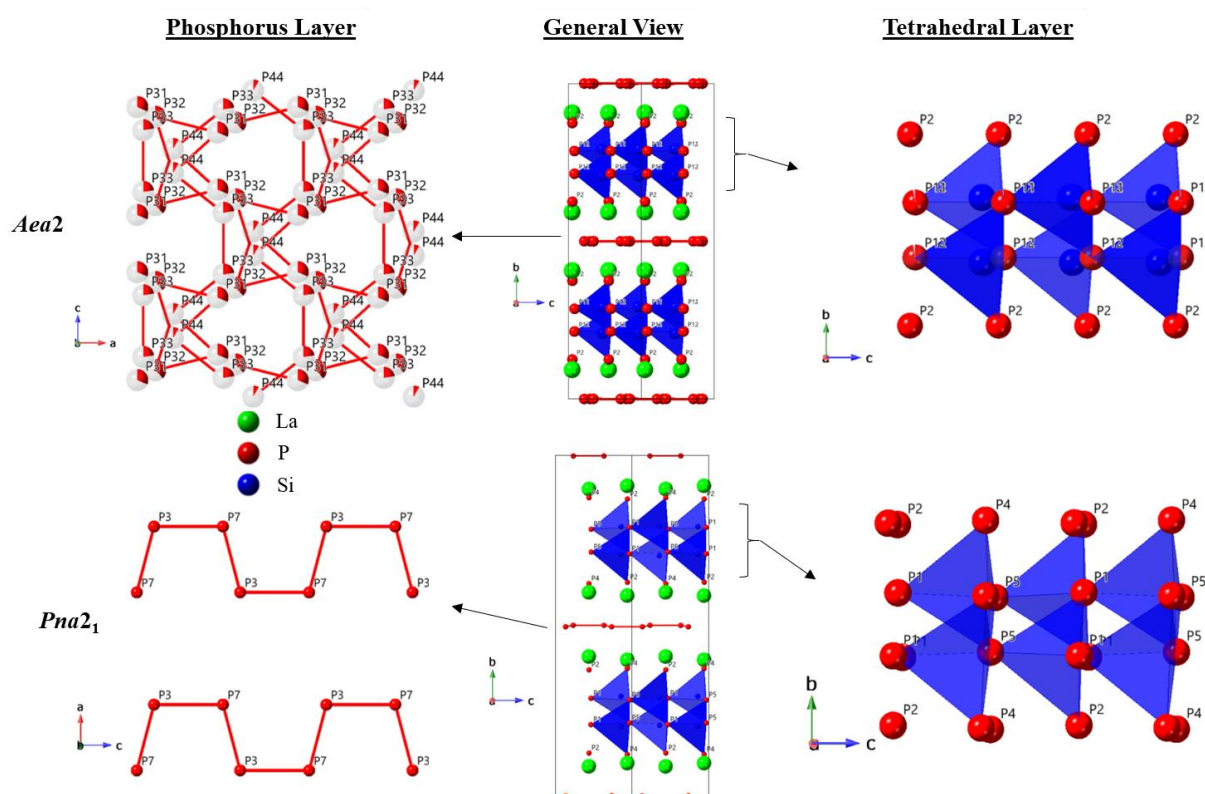


Figure S9. Crystal structures of the main two polymorphs of LaSiP_3 with labeled phosphorus positions: **(top)** Aea_2 and **(bottom)** Pna_2_1 . For the P layers, P-P bonds (lines connecting P atoms) are shown for distances in the range of 2.1 – 2.5 Å. Element legend: La - green; Si (atoms and tetrahedra) - blue; P - red (with partial occupancy).

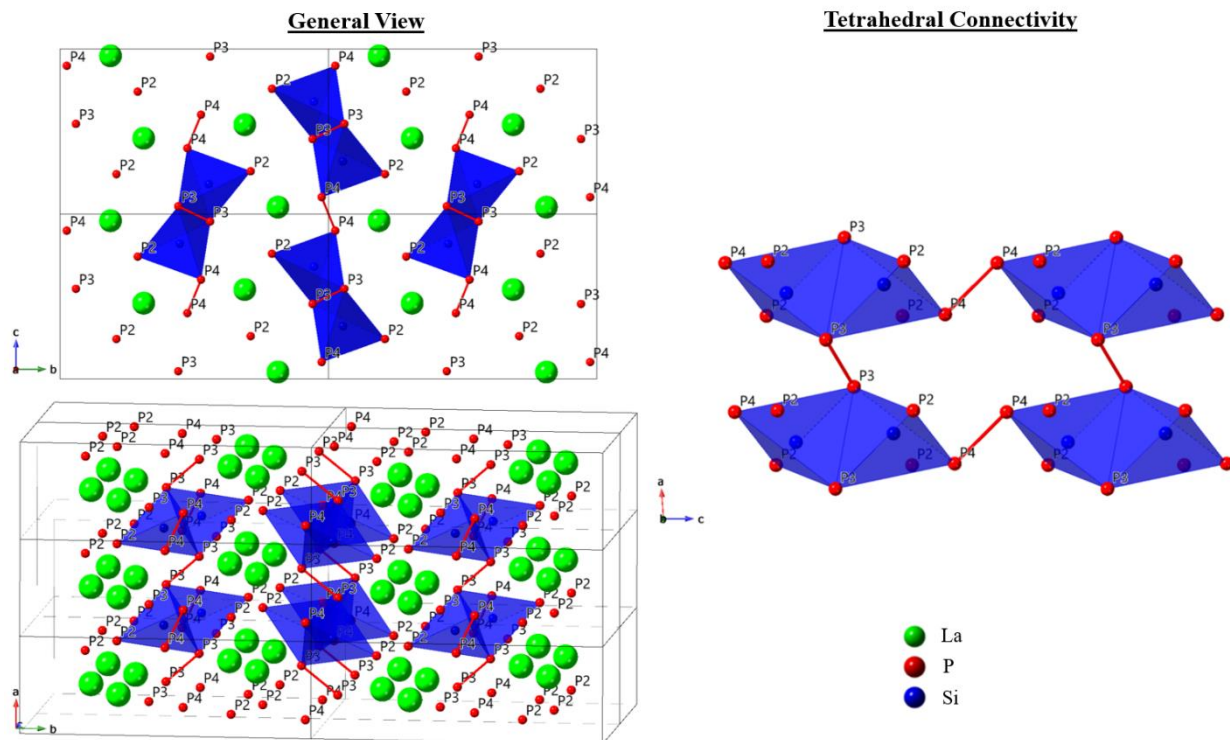


Figure S10. Crystal structure of $P2_1/c$ LaSiP_3 with labeled phosphorus positions, showing a general view as well as SiP_4 tetrahedral connectivity. Element legend: La - green; Si (atoms and tetrahedra) - blue; P – red.

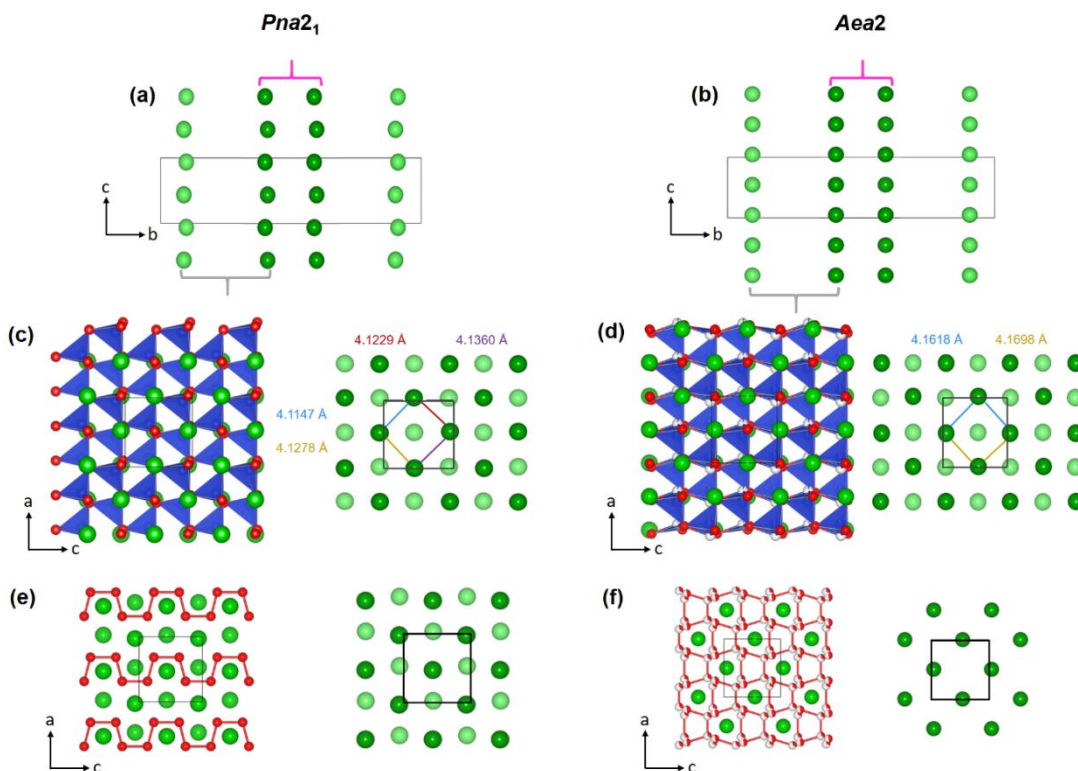


Figure S11. La layers in the *Pna2₁* (left) and *Aea2* (right) polymorphs of LaSiP₃. (a), (b) Projections down [100] direction showing slightly corrugated and in-line rows of La atoms in a single unit cell of the *Pna2₁* and *Aea2* polymorphs, respectively. Gray brackets denote stacking of a La layer, double-tetrahedral layer, and another La layer. Pink brackets denote stacking of a La layer, pnictogen layer, and another La layer. (c), (d) Projections down [010] direction highlighting the stacking of a La layer, SiP₄ double-tetrahedral layer, and an additional La layer. SiP₄ tetrahedra (blue) are removed for clarity in viewing the staggered layers of La atoms. The upper layer is shown in a dark green and the lower layer is shown in a light green. Selected bond distances are given in colors corresponding to the colors of lines connecting La atoms. (e), (f) Projections down [010] direction highlighting the stacking of a La layer, pnictogen layer, and an additional La layer. The staggering of La atoms is evident in the *Pna2₁* polymorph while La atoms are eclipsed in the *Aea2* structure. The upper layer is shown in a dark green and the lower layer is shown in a light green. Element legend - La (green), Si (blue), and P (red). A single unit cell is outlined in black.

La atoms in the layers have nearly square coordination with the nearest neighbor La atoms in the same layer. The resulting 2D plane group for La layers within the *Pna2₁* structure is *p1* due to the inequivalent distances between La atoms; however, an idealized plane group of *p4/mmm* can be assigned if the model is simplified and has similar La-La interatomic distances (**Figure S11c**). The primitive centering of the La layer's plane group is a result of the mild corrugation and stacking of La atoms. However, the flat La atoms of the *Aea2* crystal structure yield a base-centered plane group of *cm*, a distortion from an idealized *mmm* plane group due to slight differences in La-La interatomic distances (**Figure S11d**). The mild distortions of La atoms from an ideal square environment can be considered a local geometric frustration in which the La atoms struggle to find a balance between the symmetries of a tetragonal supergroup, the assigned orthorhombic space group, and a possible lower-symmetry model with long-range ordering.

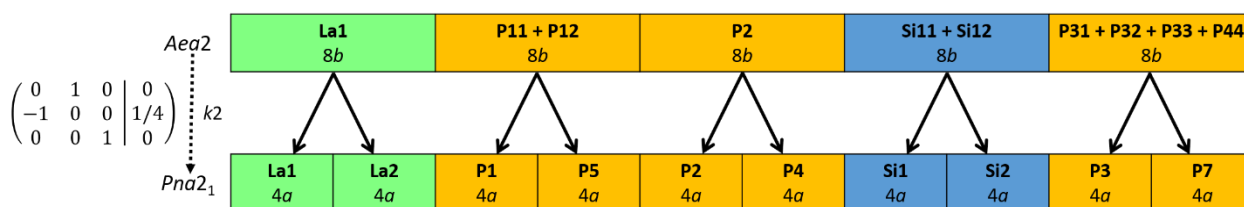


Figure S12. Relationship between $Pna2_1$ and $Aea2$ space groups with corresponding splitting of atomic positions in the main two polymorphs of $LaSiP_3$.

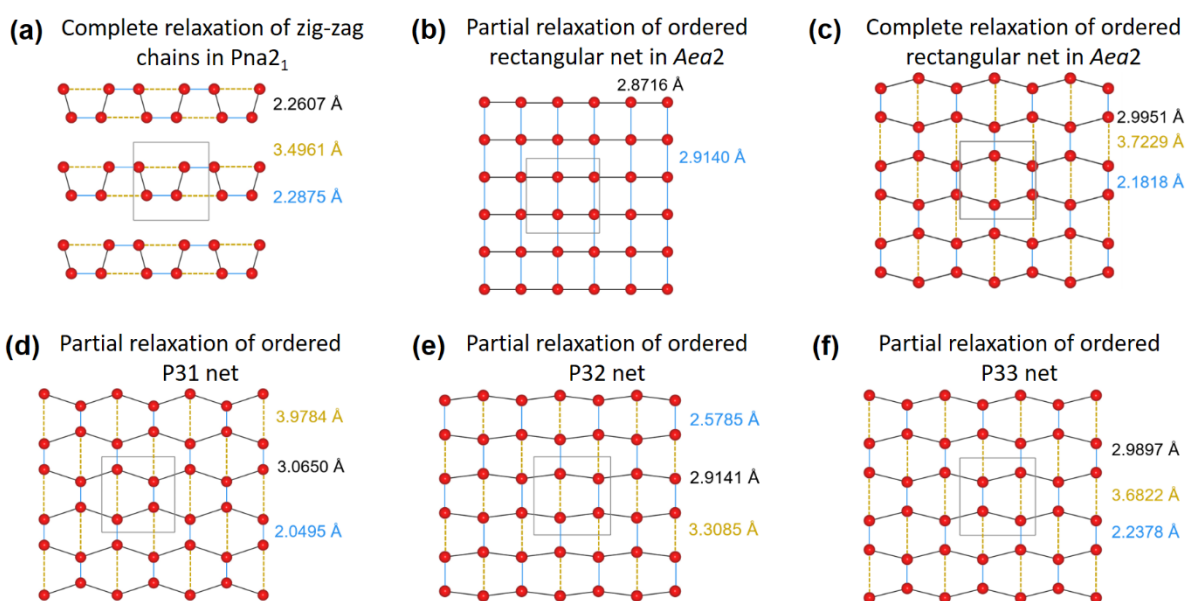
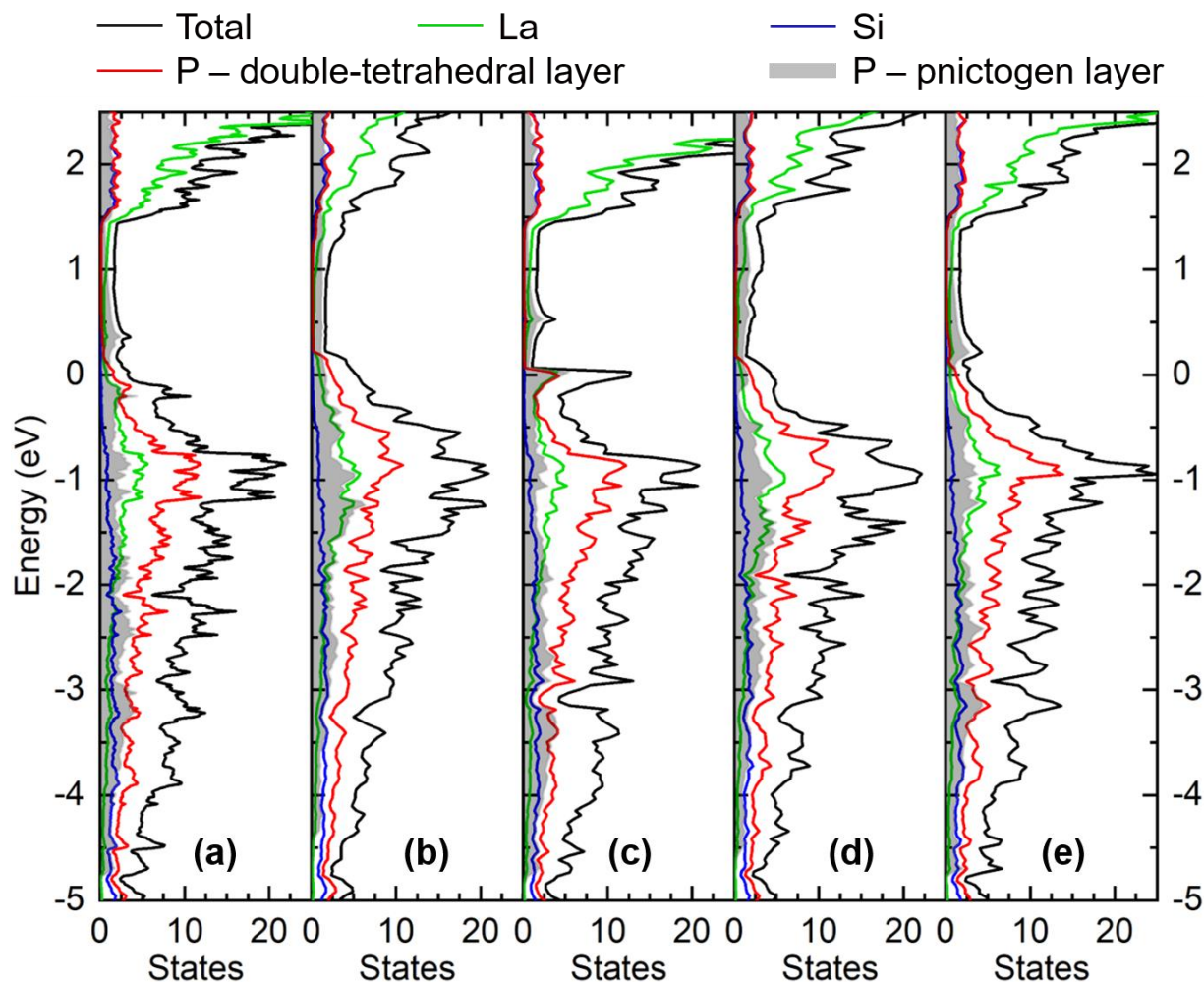


Figure S13. Interatomic distances in the pnictogen layer of VASP-relaxed structures for $Pna2_1$ and $Aea2$ $LaSiP_3$. All projections are down the $[010]$ direction. (a) The 1D cis-trans chains of P do not distort or change significantly with complete relaxation of the $Pna2_1$ crystal structure. (b) An ordered model of $Aea2$ $LaSiP_3$ was made with a rectangular net of P atoms (replacing the disordered pnictogen layer) and partially relaxed. (c) An ordered model of $Aea2$ $LaSiP_3$ with a rectangular net of P atoms (replacing the disordered pnictogen layer) was completely relaxed and found to preferentially form of P_2 dumbbells. (d-f) Partial relaxation of ordered models of $Aea2$ $LaSiP_3$ with full occupancy of either the P31, P32, or P33 sites, respectively, in the pnictogen layer were also found to form P_2 dumbbells. Element legend - P (red). A single unit cell is outlined in gray.



Model	Total Energy (eV/atom)
(a) Complete relaxation of ordered rectangular net	-5.99993
(b) Partial relaxation of ordered rectangular net	-5.94793
(c) Partial relaxation of ordered P31 net	-5.98398
(d) Partial relaxation of ordered P32 net	-5.95026
(e) Partial relaxation of ordered P33 net	-5.99094

Figure S14. Calculated DOS for five relaxed models of the *Aea2* polymorph of LaSiP_3 . (a) Model consisting of an ordered rectangular net of P atoms was completely relaxed, (b) Model consisting of an ordered rectangular net of P atoms was partially relaxed, (c) Model consisting of pnictogen layer with P31 atoms only was partially relaxed, (d) Model consisting of pnictogen layer with P32 atoms only was partially relaxed, and (e) Model consisting of pnictogen layer with P33 atoms only was partially relaxed. The total DOS is shown by the black line while the partial DOS is shown for La states (green), Si states (blue), and P states (red and gray filled). The P states are further divided into the contribution from the SiP_4 double-tetrahedral layer (red) and the P layer (gray filled). The Fermi level, indicated by the dashed black line, is the reference energy.

The DOS of the fully relaxed *Aea2* model shares many similarities to the *Pna2₁* polymorph. However, there is a distinct difference in the electronic structure near the Fermi level from -0.25 eV to 1 eV. Unlike the *Pna2₁* polymorph which has a bandgap, the Fermi level in the fully relaxed *Aea2* model falls in a pseudogap with nearby contributions coming from P in the pnictogen layer. Similar findings are reported for ZrSiS-type YbPS in which incrementally distorting the square net of P atoms into a cis-trans chain opens up the bandgap by avoiding a band crossing at the Fermi level.²⁷ The preference for chains over nets of pnictogen atoms is also observed in the crystal structures of lighter Group 15 elements and is attributed to significant s-p mixing in the band structure of these materials.²⁸

The formation of dumbbells in the *Aea2* structure is one possible substructure but is certainly not the only option.²⁷ To further probe the role of the pnictogen layer's substructure in determining the electronic structure of the *Aea2* polymorph, other models were constructed, optimized, and studied in terms of their DOS (**Figure S13** and **S14**). One such model was based on the previous simple model consisting of a rectangular net of P atoms with long hypervalent interatomic distances. This model was partially relaxed resulting in an *Aea2* structure with reasonable unit cell lattice parameters ($a = 5.8466 \text{ \AA}$, $b = 25.4229 \text{ \AA}$, $c = 5.7431 \text{ \AA}$) and retention of the rectangular net of P atoms (**Figure S13b**). Additional models were constructed based on the P31, P32, or P33 crystallographic sites and relaxed partially as well; these models retained the substructure of their pnictogen layers with reasonable lattice parameters for the unit cells (**Figure S13d-f**).

Comparing the DOS for the fully and partially relaxed *Aea2* structures (**Figure S14**) revealed that the formation of P₂ dumbbells, as opposed to maintaining hypervalent P bonding, did not eliminate the states near the Fermi level. Like the fully relaxed model, the other four models have states related to the pnictogen layer at and slightly above the Fermi level. Visually, it is clear that the DOS in **Figure S13a, e** are similar to one another and the interatomic distances in these relaxed models are also comparable. While it is anticipated that the partially relaxed P31 net model would be the least favorable model based on the relatively large number of states at the Fermi level, further investigations revealed the model with a partially relaxed rectangular net was the least favorable energetically with the highest total energy of the five *Aea2* models. The P₂ dumbbells in the P31 net model have interatomic distances that are shorter than typical P-P single bonds; however, this interaction is still more favorable than the hypervalent distances observed in the partially relaxed rectangular net model based on the total energies of the two models. Strong *s-p* mixing in a chain of P atoms within the pnictogen layer results in a shortened P-P interactions via a Peierls distortion – a known stabilizing effect which ultimately lowers the free energy of the crystal structure.²⁹

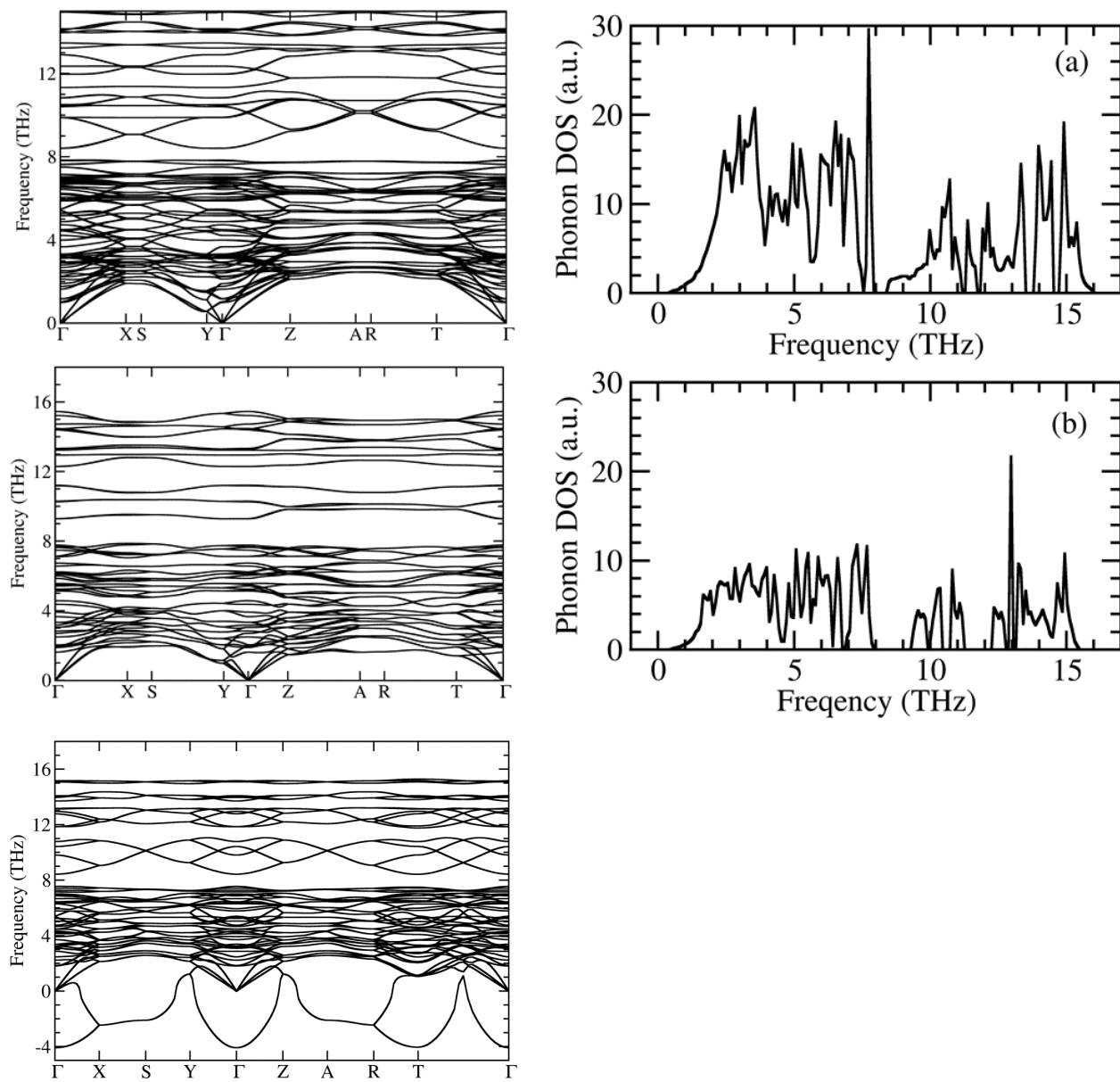


Figure S15. Phonon DOS for (top) *Pna*2₁, (middle) *P*2₁/*c*, and (bottom) fully relaxed *Aea*2 model of LaSiP₃. The latter show imaginary modes.

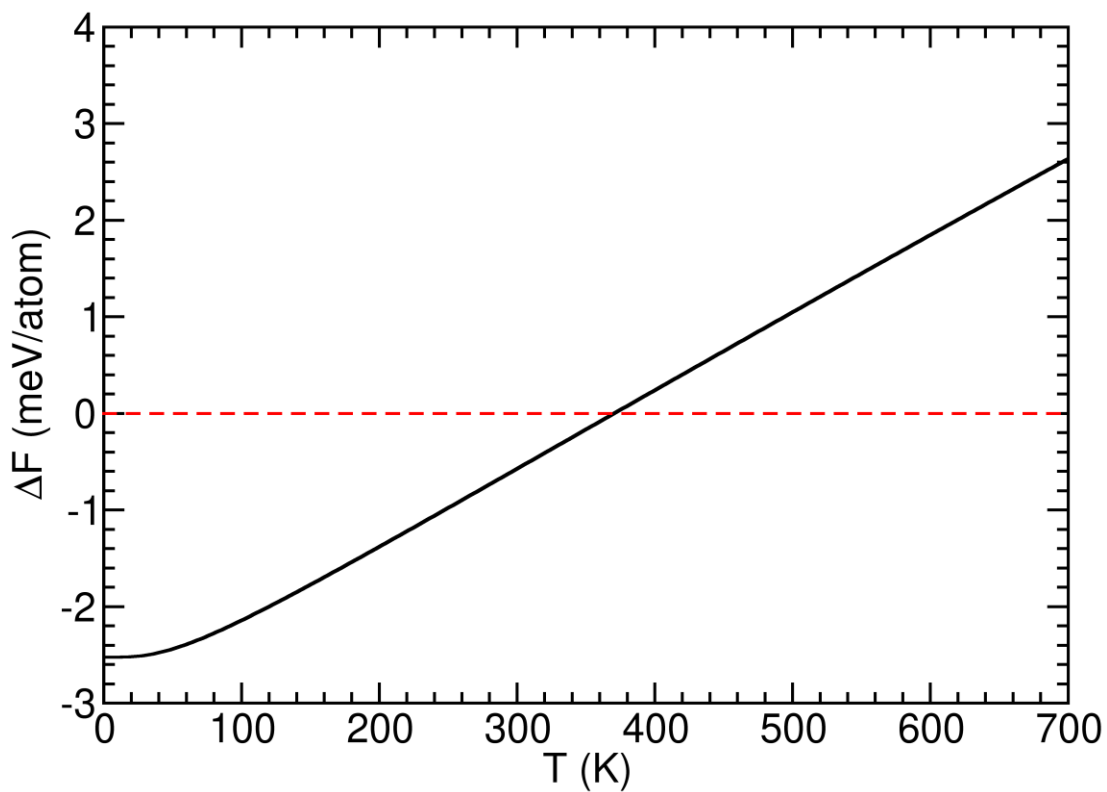


Figure S16. Free energy difference between the $Pna2_1$ and $P2_1/c$ polymorphs of $LaSiP_3$ as a function of the temperature. $\Delta F = F(Pna2_1) - F(P2_1/c)$.

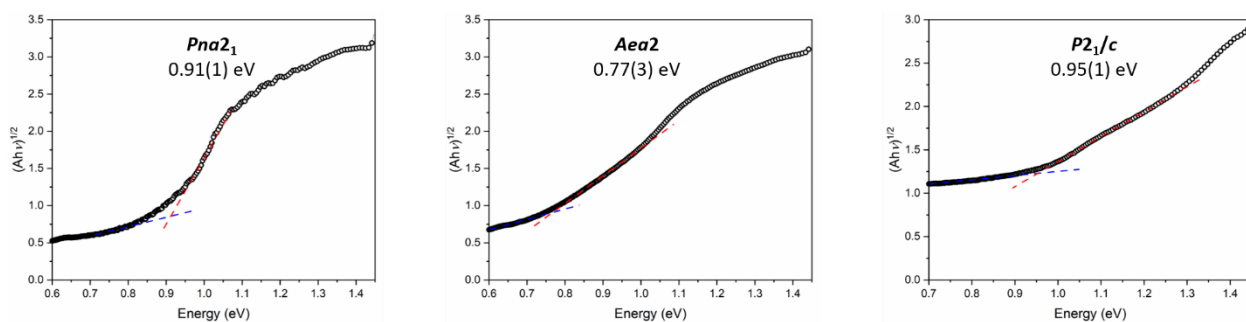


Figure S17. Tauc plots for the indirect transitions in all three polymorphs of $LaSiP_3$: $Pna2_1$, $Aea2$ and $P2_1/c$. Due to the presence of a significant Urbach tail, no definitive conclusions about the direct/indirect nature of these compounds can be made.

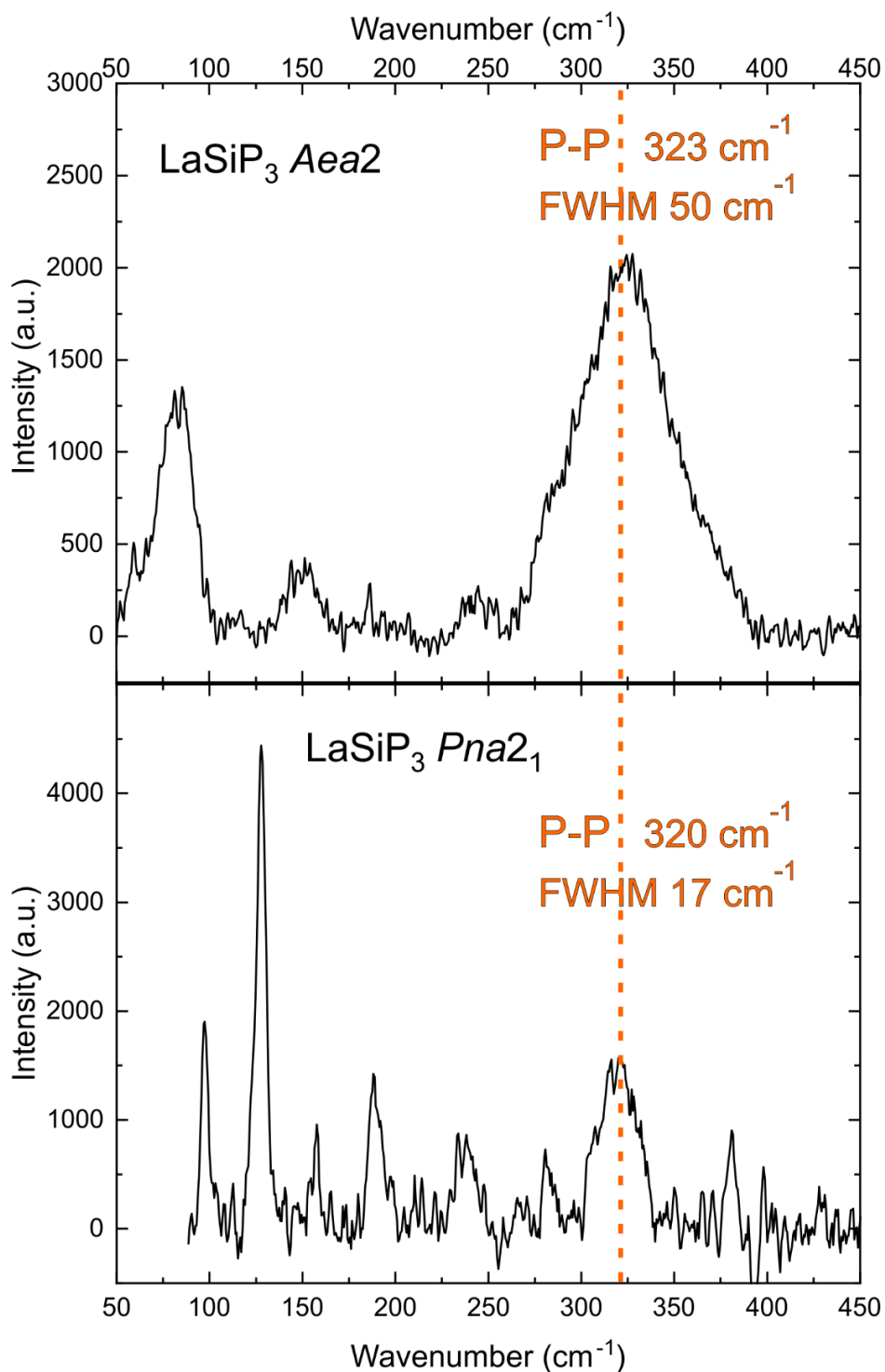
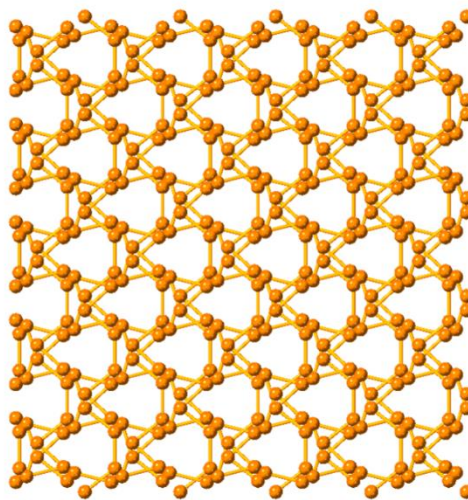
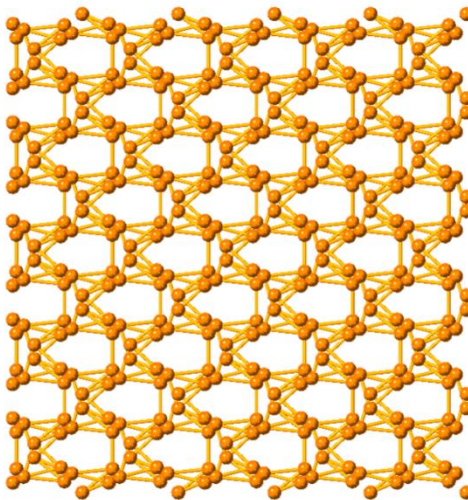


Figure S18. Unpolarized Raman spectra of LaSiP_3 polymorphs: (**top**) Aea2 , and (**bottom**) Pna2_1 . Note the vibrational band corresponding to P-P stretching becomes three times wider for the Aea2 polymorph. The modes in the Pna2_1 polymorph spectrum have been assigned based on calculations as following: 97 cm^{-1} (La-P), 128 cm^{-1} (La-P), $154/157 \text{ cm}^{-1}$ (Si-P/P-P), 189 cm^{-1} (Si-P), 198 cm^{-1} (P-P), 235 cm^{-1} (Si-P), 280 cm^{-1} (Si-P), 320 cm^{-1} (P-P), 381 cm^{-1} (P-P).

d(P-P)
2.1 – 2.4 Å



d(P-P)
2.1 – 2.5 Å



d(P-P)
2.1 – 2.7 Å

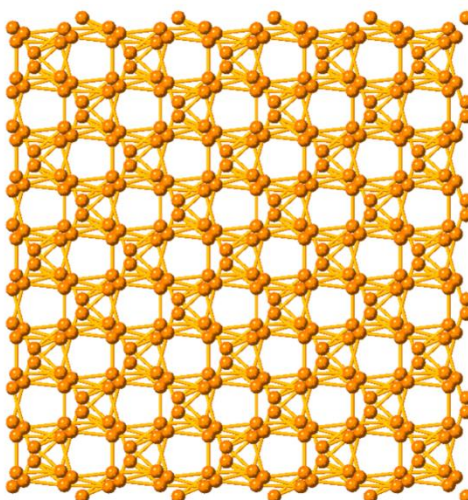


Figure S19. Different representations of P layer in the crystal structure of *Aea2* LaSiP₃ polymorph with distance cut-offs (top) 2.4 Å, (middle) 2.5 Å, and (bottom) 2.7 Å.

References

- (1) Sheldrick, G. M. A Short History of *SHELX*. *Acta Crystallogr A Found Crystallogr* **2008**, *64* (1), 112–122. <https://doi.org/10.1107/S0108767307043930>.
- (2) Toby, B. H.; Von Dreele, R. B. GSAS-II: The Genesis of a Modern Open-Source All Purpose Crystallography Software Package. *Journal of Applied Crystallography* **2013**, *46* (2), 544–549. <https://doi.org/10.1107/S0021889813003531>.
- (3) Hu, J. Z.; Alderman, D. W.; Ye, C.; Pugmire, R. J.; Grant, D. M. An Isotropic Chemical Shift-Chemical Shift Anisotropy Magic-Angle Slow-Spinning 2D NMR Experiment. *Journal of Magnetic Resonance* **1993**, *105*, 82–87.
- (4) Feike, M.; Demco, D. E.; Graf, R.; Gottwald, J.; Hafner, S.; Spiess, H. W. Broadband Multiple-Quantum NMR Spectroscopy. *Journal of Magnetic Resonance, Series A* **1996**, *122* (2), 214–221. <https://doi.org/10.1006/jmra.1996.0197>.
- (5) Grey, C. P.; Veeman, W. S. The Detection of Weak Heteronuclear Coupling between Spin 1 and Spin 1/2 Nuclei in MAS NMR; $^{14}\text{N}/\ ^3\text{C}/\ ^1\text{H}$ Triple Resonance Experiments. *CHEMICAL PHYSICS LETTERS* **1992**, *192* (4), 7.
- (6) Grey, C. P.; Vega, J. Determination of the Quadrupole Coupling Constant of the Invisible Aluminum Spins in Zeolite HY with $^1\text{H}/^{27}\text{Al}$ TRAPDOR NMR. *Journal of the American Chemical Society* **1995**, *117*, 8232–8242.
- (7) Clark, S. J.; Segall, M. D.; Pickard, C. J.; Hasnip, P. J.; Probert, M. I. J.; Refson, K.; Payne, M. C. First Principles Methods Using CASTEP. *Zeitschrift für Kristallographie - Crystalline Materials* **2005**, *220* (5/6). <https://doi.org/10.1524/zkri.220.5.567.65075>.
- (8) Pickard, C. J.; Mauri, F. All-Electron Magnetic Response with Pseudopotentials: NMR Chemical Shifts. *Phys. Rev. B* **2001**, *63* (24), 245101. <https://doi.org/10.1103/PhysRevB.63.245101>.
- (9) Yates, J. R.; Pickard, C. J.; Mauri, F. Calculation of NMR Chemical Shifts for Extended Systems Using Ultrasoft Pseudopotentials. *Phys. Rev. B* **2007**, *76* (2), 024401. <https://doi.org/10.1103/PhysRevB.76.024401>.
- (10) Vanderbilt, D. Soft Self-Consistent Pseudopotentials in a Generalized Eigenvalue Formalism. *Phys. Rev. B* **1990**, *41* (11), 7892–7895. <https://doi.org/10.1103/PhysRevB.41.7892>.
- (11) Perdew, J. P.; Ruzsinszky, A.; Csonka, G. I.; Vydrov, O. A.; Scuseria, G. E.; Constantin, L. A.; Zhou, X.; Burke, K. Restoring the Density-Gradient Expansion for Exchange in Solids and Surfaces. *Phys. Rev. Lett.* **2008**, *100* (13), 136406. <https://doi.org/10.1103/PhysRevLett.100.136406>.
- (12) Profeta, M.; Mauri, F.; Pickard, C. J. Accurate First Principles Prediction of ^{17}O NMR Parameters in SiO_2 : Assignment of the Zeolite Ferrierite Spectrum. *J. Am. Chem. Soc.* **2003**, *125* (2), 541–548. <https://doi.org/10.1021/ja027124r>.
- (13) Charpentier, T. The PAW/GIPAW Approach for Computing NMR Parameters: A New Dimension Added to NMR Study of Solids. *Solid State Nuclear Magnetic Resonance* **2011**, *40* (1), 1–20. <https://doi.org/10.1016/j.ssnmr.2011.04.006>.
- (14) Bonhomme, C.; Gervais, C.; Babonneau, F.; Coelho, C.; Pourpoint, F.; Azaïs, T.; Ashbrook, S. E.; Griffin, J. M.; Yates, J. R.; Mauri, F.; Pickard, C. J. First-Principles Calculation of NMR Parameters Using the Gauge Including Projector Augmented Wave Method: A Chemist's Point of View. *Chem. Rev.* **2012**, *112* (11), 5733–5779. <https://doi.org/10.1021/cr300108a>.
- (15) Mac Dougall, J. E.; Eckert, H.; Stucky, G. D.; Herron, N.; Wang, Y.; Moller, K.; Bein, T.; Cox, D. Synthesis and Characterization of Group III-V Semiconductor Clusters: Gallium Phosphide GaP in Zeolite Y. *J. Am. Chem. Soc.* **1989**, *111* (20), 8006–8007. <https://doi.org/10.1021/ja00202a047>.
- (16) Duncan, T. M.; Karlicek, R. F.; Bonner, W. A.; Thiel, F. A. A ^{31}P Nuclear Magnetic Resonance Study of InP, GaP and InGaP. *Journal of Physics and Chemistry of Solids* **1984**, *45* (4), 389–391. [https://doi.org/10.1016/0022-3697\(84\)90145-8](https://doi.org/10.1016/0022-3697(84)90145-8).

- (17) Kresse, G.; Furthmüller, J. Efficient Iterative Schemes for Ab Initio Total-Energy Calculations Using a Plane-Wave Basis Set. *Phys. Rev. B* **1996**, *54* (16), 11169–11186. <https://doi.org/10.1103/PhysRevB.54.11169>.
- (18) Kresse, G.; Joubert, D. From Ultrasoft Pseudopotentials to the Projector Augmented-Wave Method. *Phys. Rev. B* **1999**, *59* (3), 1758–1775. <https://doi.org/10.1103/PhysRevB.59.1758>.
- (19) Blöchl, P. E. Projector Augmented-Wave Method. *Phys. Rev. B* **1994**, *50* (24), 17953–17979. <https://doi.org/10.1103/PhysRevB.50.17953>.
- (17) Perdew, J. P. Density Functional Theory and the Band Gap Problem. *Int. J. Quantum Chem.* **1985**, *28* (S19), 497–523. <https://doi.org/10.1002/qua.560280846>.
- (21) Perdew, J. P.; Burke, K.; Ernzerhof, M. Generalized Gradient Approximation Made Simple. *Phys. Rev. Lett.* **1996**, *77* (18), 3865–3868. <https://doi.org/10.1103/PhysRevLett.77.3865>.
- (22) Blöchl, P. E.; Jepsen, O.; Andersen, O. K. Improved Tetrahedron Method for Brillouin-Zone Integrations. *Phys. Rev. B* **1994**, *49* (23), 16223–16233. <https://doi.org/10.1103/PhysRevB.49.16223>.
- (23) Monkhorst, H. J.; Pack, J. D. Special Points for Brillouin-Zone Integrations. *Phys. Rev. B* **1976**, *13* (12), 5188–5192. <https://doi.org/10.1103/PhysRevB.13.5188>.
- (24) FINDSYM <https://stokes.byu.edu/iso/findsym.php> (accessed Nov 18, 2020).
- (25) Stokes, H. T.; Hatch, D. M. *FINDSYM*: Program for Identifying the Space-Group Symmetry of a Crystal. *J Appl Crystallogr* **2005**, *38* (1), 237–238. <https://doi.org/10.1107/S0021889804031528>.
- (26) Togo, A.; Tanaka, I. First Principles Phonon Calculations in Materials Science. *Scripta Materialia* **2015**, *108*, 1–5. <https://doi.org/10.1016/j.scriptamat.2015.07.021>.
- (27) Tremel, W.; Hoffmann, R. Square Nets of Main-Group Elements in Solid-State Materials. *J. Am. Chem. Soc.* **1987**, *109* (1), 124–140. <https://doi.org/10.1021/ja00235a021>.
- (28) Seo, D. K.; Hoffmann, R. What Determines the Structures of the Group 15 Elements? *Journal of Solid State Chemistry* **1999**, No. 147, 26–37.
- (29) Papoian, G. A.; Hoffmann, R. Hypervalent Bonding in One, Two, and Three Dimensions: Extending the Zintl-Klemm Concept to Nonclassical Electron-Rich Networks. *Angew. Chem. Int. Ed.* **2000**, 41.